

One registration multi-atlas-based pseudo-CT generation for attenuation correction in PET/MRI

Hossein Arabi¹ · Habib Zaidi^{1,2,3,4}

Received: 18 March 2016 / Accepted: 10 May 2016 / Published online: 3 June 2016
© Springer-Verlag Berlin Heidelberg 2016

Abstract

Purpose The outcome of a detailed assessment of various strategies for atlas-based whole-body bone segmentation from magnetic resonance imaging (MRI) was exploited to select the optimal parameters and setting, with the aim of proposing a novel one-registration multi-atlas (ORMA) pseudo-CT generation approach.

Methods The proposed approach consists of only one online registration between the target and reference images, regardless of the number of atlas images (N), while for the remaining atlas images, the pre-computed transformation matrices to the reference image are used to align them to the target image. The performance characteristics of the proposed method were evaluated and compared with conventional atlas-based attenuation map generation strategies (direct registration of the entire atlas images followed by voxel-wise weighting (VWW) and arithmetic averaging atlas fusion). To this end, four different positron emission tomography (PET) attenuation maps were generated via arithmetic averaging and VWW scheme using both direct registration and ORMA approaches as well

as the 3-class attenuation map obtained from the Philips Ingenuity TF PET/MRI scanner commonly used in the clinical setting. The evaluation was performed based on the accuracy of extracted whole-body bones by the different attenuation maps and by quantitative analysis of resulting PET images compared to CT-based attenuation-corrected PET images serving as reference.

Results The comparison of validation metrics regarding the accuracy of extracted bone using the different techniques demonstrated the superiority of the VWW atlas fusion algorithm achieving a Dice similarity measure of 0.82 ± 0.04 compared to arithmetic averaging atlas fusion (0.60 ± 0.02), which uses conventional direct registration. Application of the ORMA approach modestly compromised the accuracy, yielding a Dice similarity measure of 0.76 ± 0.05 for ORMA-VWW and 0.55 ± 0.03 for ORMA-averaging. The results of quantitative PET analysis followed the same trend with less significant differences in terms of SUV bias, whereas massive improvements were observed compared to PET images corrected for attenuation using the 3-class attenuation map. The maximum absolute bias achieved by VWW and VWW-ORMA methods was 06.4 ± 5.5 in the lung and 07.9 ± 4.8 in the bone, respectively.

Conclusions The proposed algorithm is capable of generating decent attenuation maps. The quantitative analysis revealed a good correlation between PET images corrected for attenuation using the proposed pseudo-CT generation approach and the corresponding CT images. The computational time is reduced by a factor of $1/N$ at the expense of a modest decrease in quantitative accuracy, thus allowing us to achieve a reasonable compromise between computing time and quantitative performance.

Keywords PET/MRI · Hybrid imaging · Attenuation correction · Attenuation map · Atlas

✉ Habib Zaidi
habib.zaidi@hcuge.ch

¹ Division of Nuclear Medicine and Molecular Imaging, Geneva University Hospital, CH-1211 Geneva 4, Switzerland

² Geneva Neuroscience Center, Geneva University, CH-1205 Geneva, Switzerland

³ Department of Nuclear Medicine and Molecular Imaging, University of Groningen, University Medical Center Groningen, 9700 RB Groningen, Netherlands

⁴ Department of Nuclear Medicine, University of Southern Denmark, DK-500 Odense, Denmark

Introduction

Hybrid PET/MRI (positron emission tomography/magnetic resonance imaging) is establishing itself as a promising multi-modality imaging technology and is expected to open new insight in clinical diagnostic imaging [1]. In essence, the capability of MRI to provide higher soft-tissue contrast compared to CT, its ability of multiparametric imaging through the various sequences and, above all the absence of radiation exposure, has made it a promising candidate for combination with PET scanning. The growing technical and clinical research interests are directed towards the development of compact concurrent PET/MRI systems with high-temporal-resolution time of flight capabilities, as well as addressing the challenges of quantitative imaging [2]. Despite the promise of PET/MRI, how to best define a clear and unambiguous roadmap in terms of clinical applications of this technology is still being debated [3–5]. In addition, correcting the PET emission data for attenuation is still a major challenge since there is no correlation between MR intensity and attenuation coefficients of biological tissues [6, 7]. Nonetheless, a number of attenuation map generation methods have been proposed, including MR image segmentation techniques for brain [8] and whole-body imaging [9, 10], atlas and machine learning approaches for brain [11] and whole-body imaging [12, 13], the use of dedicated MRI sequences, such as ultra-short echo (UTE) [14, 15] or zero time echo (ZTE) [16] to extract bony structures, and the joint estimation of emission and transmission maps from the only the emission data [17, 18].

Tissue class segmentation techniques are the most widely used on commercial PET/MRI scanners in the clinical setting. Ignoring bones is the major limitation of commonly used segmentation approaches since segmenting bones from conventional MRI sequences is a prohibitively difficult task, particularly in whole-body imaging [6, 7]. UTE/ZTE MRI sequences enable identification of a separate bone class owing to the distinct contrast between air and bone; however, the relatively long scanning time has limited its usage to single-bed acquisition protocols, such as brain imaging [14]. An alternative option to include bony structures in MRI-based attenuation maps is to use prior knowledge provided by atlas registration [12, 19]. Promising results have been reported using atlas registration techniques for attenuation correction in the head region [12, 19–26]. Most of the proposed attenuation map generation approaches considering bone in whole-body PET/MRI rely on prior information provided by atlas images to delineate bony structures [12, 27–29]. Hofmann et al. used a machine-learning technique based on the registration of multiple MRI/CT pairs to the patient's MRI [12]. Bezrukov et al. modified the original technique by using bone probability maps to address signal loss arising from metal object artifacts in MR images and to reduce the processing time [27]. More recently, Arabi and Zaidi further improved the performance of

this approach by introducing a dedicated regression kernel for lung attenuation estimation and enhancing bone identification through atlas sorting [13]. Still the computational time required for multiple atlas registration and training of the algorithm is considered to be the main limitation of this category of techniques. Moreover, comparative studies have demonstrated that there is still scope for improving further their accuracy [30, 31]. To reduce the processing time, Marshall et al. proposed a scheme enabling identification of the most similar subject to the target image in terms of body geometry [29].

In a previous work, we compared a number of atlas-based segmentation techniques for bone segmentation from whole-body MRI [31]. As a result, an optimized segmentation algorithm was devised which outperformed previous methods of whole-body attenuation map generation in terms of bone extraction accuracy. The aim of this work is to evaluate the accuracy of the proposed whole-body bone segmentation method using clinical PET/MRI studies and, more importantly, to propose a novel one-registration multiple-atlas (ORMA) pseudo-CT generation approach that drastically reduces computation time. The proposed approach requires only one online registration for each target subject regardless of the number of used atlas images (N) and at the same time benefits from the information available from multiple atlas datasets.

The performance of the proposed method was compared with direct registration of the entire set of atlas images to the target followed by arithmetic averaging and voxel-wise weighting (VWW) atlas fusion schemes. The resulting pseudo-CT images were evaluated in terms of accuracy of extracted bone using standard segmentation validation measures and quantitative analysis of tracer uptake in corresponding attenuation-corrected PET images.

Materials and methods

PET/MRI/CT data acquisition and reconstruction

The patient population in this study consists of 23 patients (15 men and eight women); mean age \pm SD = 60 ± 8 y, referred to our department for whole-body ^{18}F -FDG PET/MRI examinations for staging of head and neck malignancies. The study protocol was approved by the institutional ethics committee and all patients gave their written informed consent. A single injection of ^{18}F -FDG (371 ± 23 MBq) was administered and patients underwent MRI examinations on the Ingenuity TF PET/MRI system (Philips Healthcare, Cleveland, OH) [32]. The aforementioned PET/MR scanner utilizes a 3-class segmentation attenuation map derived from a 3D multi-stack spoiled T1-weighted MRI (flip angle 10° , TE 2.3 ms, TR 4.1 ms) comprising background air 0.0 cm^{-1} ($-1,000$ HU), lung 0.022 cm^{-1} (-770 HU), and soft-tissue 0.096 cm^{-1} (0 HU) for PET attenuation correction [10]. The 3-class

attenuation map technique is also evaluated in this work as a common attenuation correction approach used in the clinic. Our MRI-guided pseudo-CT generation approach uses a whole-body Dixon 3D volumetric interpolated T1-weighted sequence acquired using the following parameters: flip angle 10° , TE 11.1 ms, TE 22.0 ms, TR 3.2 ms, $450 \times 354 \text{ mm}^2$ transverse FOV, $0.85 \times 0.85 \times 3 \text{ mm}^3$ voxel size. The total acquisition time for each patient was 2 min and 17 s and fat-only, water-only, out-phase, and in-phase images were produced separately.

After PET/MRI scan completion, PET/CT scanning was performed on a Biograph 64 True Point scanner (Siemens Healthcare, Erlangen, Germany). After patient positioning and a localization scout scan, an unenhanced CT scan (120 kVp, 180 mAs, 24×1.5 collimation, a pitch of 1.2, and 1 s per rotation) was performed for the purpose of attenuation correction and anatomic localization. PET data acquisition started 146.2 ± 20 min post-injection with 3 min per bed position for a total of 5–6 bed positions, resulting in a total acquisition time of 15–18 min. CT-based attenuation-corrected PET data (PET/CTAC) of the PET/CT scans served as reference for quantitative evaluation of PET images corrected using the various attenuation maps. Both T1-weighted and Dixon MR images were non-rigidly aligned to the corresponding CT images using the elastix package [33], as described in a previous study [34]. PET images corrected for attenuation using the different techniques were reconstructed using the ordinary Poisson, ordered subset-expectation maximization (OP-OSEM) iterative reconstruction algorithm implemented in the e7 tools (Siemens) using default parameters (four iterations, eight subsets, and a post-processing Gaussian kernel with a full-width half-maximum (FWHM) of 5 mm).

Data preprocessing

The high level of noise, corruption from the low-frequency bias field inhomogeneity, and inter-patient intensity non-uniformity are among the weaknesses of short acquisition time MR sequences developed chiefly for attenuation correction, which can affect the performance of the registration procedure and local image similarity measurement. These factors have even more profound influence on image similarity analysis since the artificial intensity variation between MR images can directly affect the final outcome. To alleviate the impact of these factors, the following processing was performed on MR in-phase images.

In the first step, noise suppression was achieved by gradient anisotropic diffusion filtering [35]. This filter blurs over regions where the gradient magnitude is relatively small (homogenous regions) but diffuses little over areas of the image where the gradient magnitude is large (i.e., edges). Therefore, anatomical regions are blurred but their edges are less blurred. The anisotropic filtering parameters are conductance=4,

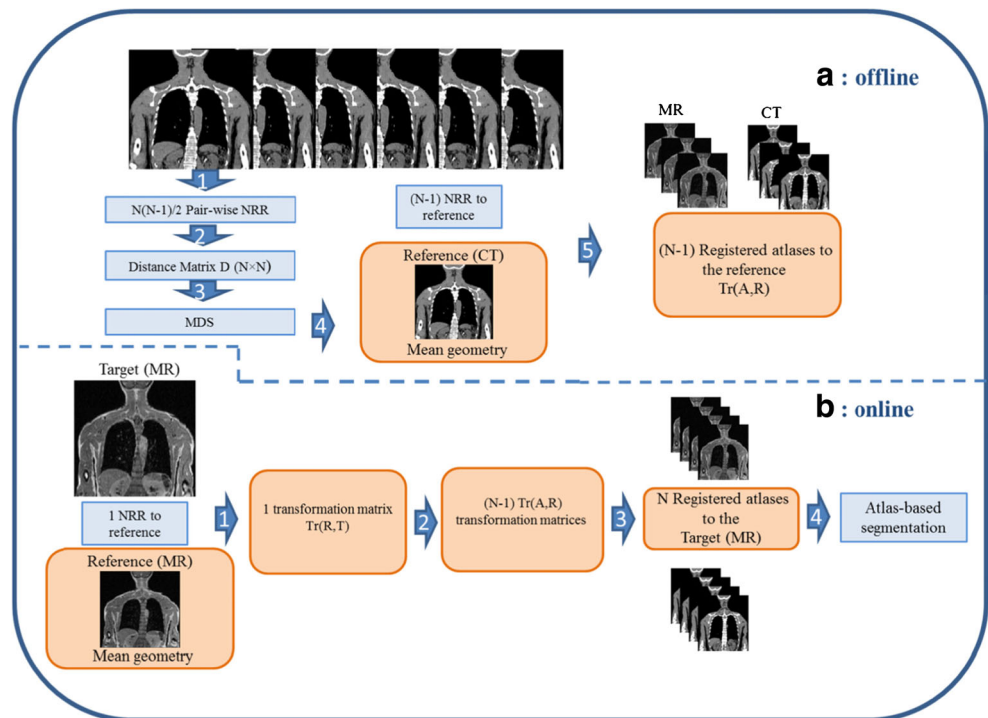
iteration=10 and time step=0.01. An N4 bias field correction algorithm [36] was employed to cancel out intra-patient intensity inhomogeneity using the following parameters: B-spline grid resolution=400, number of iteration=200 (at each grid resolution), convergence threshold=0.001, B-spline order=3, spline distance=400, number of Histograms=256 and shrink factor=3. The presence of low-frequency intensity non-uniformity within a subject, known as bias field or illumination inhomogeneity, is considered as a potential confounder in various image analysis tasks. Bias field correction minimizes the intensity inhomogeneity within an MR image caused by the non-uniform magnetic field in MR imaging. Inter-patient intensity inhomogeneity was handled through histogram matching [37] using the following settings: histogram level=1,024 and match points=128. To obtain the best result from histogram matching, it is recommended to exclude background air voxels of both reference and target images before processing.

Mean geometry patient

The first step required for implementation of the ORMA pseudo-CT generation algorithm is the determination of the mean geometry of the patient population. The common practice to create an atlas representing a population is to pick a reference patient image to which other patient images will be aligned, in such a way that the reference image coordinates act as a common spatial frame. The major drawback of this approach is that the resulting atlas would be inherently biased towards the chosen reference image. For instance, when the reference image happens to be an extreme case of the population, the resulting common spatial frame does not adequately represent the common population geometry. In this case, warping a query image into the reference space may lead to flawed outcome since the geometric distance that the query image has to travel to reach the reference spatial frame is not optimal compared to the case of reaching an atlas residing at the mean geometry of the population. Therefore, determining the closest patient to the mean geometry of the population is thought to be an essential prerequisite step.

The first step needed to determine the mean geometry of the population includes pair-wise deformable alignment of the entire set of patient images to each other, which requires $N(N-1)/2$ registrations (N is the number of atlases). Finding the patient with mean population geometry is performed offline and only once on CT images (Fig. 1). The $N(N-1)/2$ non-rigid registrations were performed by combining affine and non-rigid alignment based on the advanced Mattes mutual information [38] implemented in the elastix package [33] by considering the following settings: interpolate: thin-plate spline, optimizer: standard gradient decent, image pyramid schedule: (32 16 8 4 2 2), grid spacing schedule (32.0 32.0

Fig. 1 Flowchart describing the different steps involved in the implementation of the proposed one-registration multiple-atlas (ORMA) pseudo-CT generation approach



16.0 8.0 4.0 2.0), maximum number of iterations (8192 4096 4096 2048 1024 1024), number of histogram bins: 64. Given the $N(N-1)/2$ geometric transform matrices between patient images, the geometric distance between each pair of images can be measured by the roughness of the geometric transform. Here, we define the geometric distance between two images on the basis of the bending energy, which is the sum of squared second partial derivatives of the geometric distance, as described in [39]. The analytic formula used to calculate the bending energy for the thin-plate spline algorithm is given elsewhere [40]. The patient image residing at the mean population geometry has the minimum sum of distances to other images. Determining the closest image to the mean geometry is possible if all the relative locations of the population are known. In this work, the geometric distances obtained from pair-wise registration of the atlas images were used as surrogates of image distances. Given the relative distance of the atlas images, multidimensional scaling (MDS) was exploited to determine the mean geometry subject. MDS defines a new coordinate system in which the absolute distance of each atlas image to the origin of the new coordinate system can be calculated. The subject residing at the minimum distance to the origin in the new coordinate system is defined as the reference image (Fig. 2). More details about the MDS procedure are provided in the Appendix.

Given a reference image, all the remaining subject images are non-rigidly warped (applying the aforementioned registration procedure) to the reference image spatial coordinates. All these procedures are performed offline as illustrated in Fig. 1. At the end of this step, $(N-1)$ transformation matrices $Tr(A,R)$

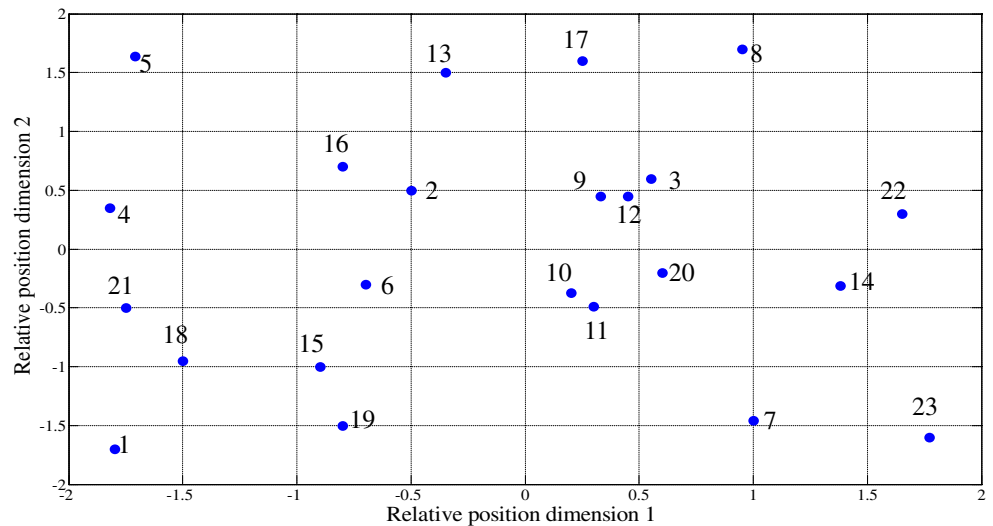
mapping the atlas images (A) to the selected reference image (R) are produced.

ORMA pseudo-CT generation procedure

The underlying idea behind the ORMA pseudo-CT generation approach is the combination of the pre-computed transformation matrices, $Tr(A,R)$, with the reference to target image transform matrix, $Tr(R,T)$, to transform all images of the atlas dataset to the target image spatial coordinate (Fig. 1). $Tr(R,T)$ obtained from online registration between the reference and target image is combined with the pre-computed transformation matrices $Tr(A,R)$ to map the $N-1$ MR images to the target image. The same transformation is applied to the corresponding CT images. This produces N pairs of MR/CT images aligned to the target MR image ($N-1$ through the indirect and 1 through direct registration), thus allowing the generation of an atlas-based pseudo-CT attenuation map. The proposed method requires only one online registration and benefits from the anatomical variability provided by multiple atlas images.

The performance of the ORMA pseudo-CT generation approach was assessed through comparison with direct registration of the entire set of atlas images to the target subject to evaluate the loss in accuracy. A leave-one-out cross-validation framework was employed for all patient datasets. Two commonly used atlas fusion schemes were adopted for attenuation map generation: arithmetic averaging and voxel-wise weighting (VWW).

Fig. 2 Relative locations of 23 subject images obtained by multi-dimensional scale (MDS) where the mean location is sited at coordinate (0,0) and the closest image to the mean is determined to be atlas number 10



Arithmetic averaging consists of simple averaging of all the aligned atlas CT images:

$$Average = \frac{1}{N} \sum_{n=1}^N Tr(CT)_n \tag{1}$$

where $Tr(CT)_n$ indicates the n th directly aligned atlas CT to the target image. Similarly, the average of atlas images using the ORMA framework is obtained by:

$$ORMA\ average = \frac{1}{N} \sum_{n=1}^N ORMA(CT)_n \tag{2}$$

The second approach incorporates VWW based on image similarity measurement within patches of voxels to mitigate the impact of non-systematic registration errors [42, 43]. In the VWW atlas fusion approach, the local similarity between the target and each of the atlas images is commonly measured using normalized mutual information (NMI), local normalized cross-correlation (LNCC), or mean square distance (MSD) similarity criteria. In our previous study [31], we addressed the optimization aspect of VWW atlas fusion based on the accuracy of bone extraction in whole-body MR imaging using the same datasets. The obtained optimal parameters and setting are employed here to generate pseudo-CT attenuation maps. The reference above concluded that the MSD image similarity measure outperformed the other aforementioned similarity criteria. The MSD between two patches of atlas and target images is calculated considering the following equation:

$$MSD_D(x) = \frac{|D|}{\sum_{x \in D} |T(x) - Tr(MR(x))_n|^2} \tag{3}$$

where, T is the MR image of the target subject, $Tr(.)$ indicates the transformation of the n th MR atlas to the target image, D stands for the neighboring voxel in the vicinity of the central

voxel x and $|D|$ represents the cardinality of D . The obtained optimal patch size (D) for calculation of the MSD similarity was 5 mm, corresponding to the edge of a cube centered at x . Since the range of calculated similarity measures can vary quite dramatically between subjects and locations, which may adversely affect the atlas fusion process, a ranking scheme was employed whereby the similarity measure value for each transformed atlas is ranked across all atlases [44]. Let's suppose that ranked atlases based on similarity measurements on patch D are denoted $R(n,x)_D$, and the conversion to appropriate weights is performed by applying an exponential decay function:

$$w(x)_n = e^{-aR(n,x)_D} \tag{4}$$

By adopting a ranking scheme, the training subject at voxel x that best matches the target subject is assigned a weight of 1 whereas the training subject presenting with the second best match is assigned a weight e^{-a} and so on. Thus, the pseudo-CT generation can be carried out by including the weighting factor w_n in the following equation:

$$\begin{aligned} VWW(x) &= \frac{1}{N_r} \sum_{n=1}^N w(x)_n \times Tr(CT(x))_n \quad \text{subject to } N_r \\ &= \sum_{n=1}^N w(x)_n \end{aligned} \tag{5}$$

$Tr(.)$ used to transform atlas images to the target spatial coordinates can be generated through either direct registration or using the ORMA approach. The resulting pseudo-CTs are referred to as VWW and ORMA-VWW, respectively. The voxel-wise atlas fusion introduces the free parameter (a), whose value after optimization was equal to 1 [31].

Data analysis

First, the attenuation maps obtained using the four different attenuation map generation strategies (arithmetic averaging and VWW using direct registration, ORMA-average, and ORMA-VWW) were evaluated based on the accuracy of extracted whole-body bone (obtained by thresholding at 140 HU). Bone identification accuracy was assessed using five volume/distance-based measures, including the Dice similarity (DSC) [45], relative volume difference (RVD) [30], Jaccard similarity (JC) [30], sensitivity (S) [46], and mean absolute surface distance (MASD) [47].

$$\begin{aligned}
 DSC(C, P) &= \frac{2|C \cap P|}{|C| + |P|}, RVD(C, P) \\
 &= 100 \times \frac{|C| - |P|}{|P|}, JC(C, P) \\
 &= \frac{|C \cap P|}{|P|}, MASD(C, P) \\
 &= \frac{d_{ave}(S_C, S_P) + d_{ave}(S_P, S_C)}{2} \quad (6)
 \end{aligned}$$

where C and P denote segmented bone from the reference CT and generated pseudo-CT images, respectively.

$d_{ave}(S_C, S_P)$ computes the average direct surface distance from all points on the reference bone surface S_C to the segmented bone surface S_P . Paired t -test analysis was used to determine if two datasets were different from each other, and the obtained results were considered statistically significant if the p -value was less than 0.05.

In addition to bone extraction, the accuracy of the generated attenuation maps was assessed in terms of lung volume overlap and air cavities identification. To this end, the lungs and air cavities in the head region were segmented separately on each attenuation map followed by application of the segmentation metrics described above to report the results. The ITK-SNAP image processing software [48] initialized by user-specified seeds was used to segment the lungs. Thereafter, the mean linear attenuation coefficient of the lungs produced by the different methods was calculated and compared to the reference value derived from CT images.

Quantitative analysis of tracer uptake was also performed on PET images corrected for attenuation using the various pseudo-CT attenuation maps. To this end, the raw PET data of the PET/CT scan were used to assess the performance of five different MRI-guided attenuation correction techniques including direct registration and arithmetic averaging (PET_Ave), ORMA plus arithmetic averaging (PET_ORMA-Ave), direct

Fig. 3 Representative slice showing (a) reference CT, and MRI-guided attenuation maps: (b) 3-class, (c) Average, (d) VWW, (e) ORMA-average and (g) ORMA-VWW

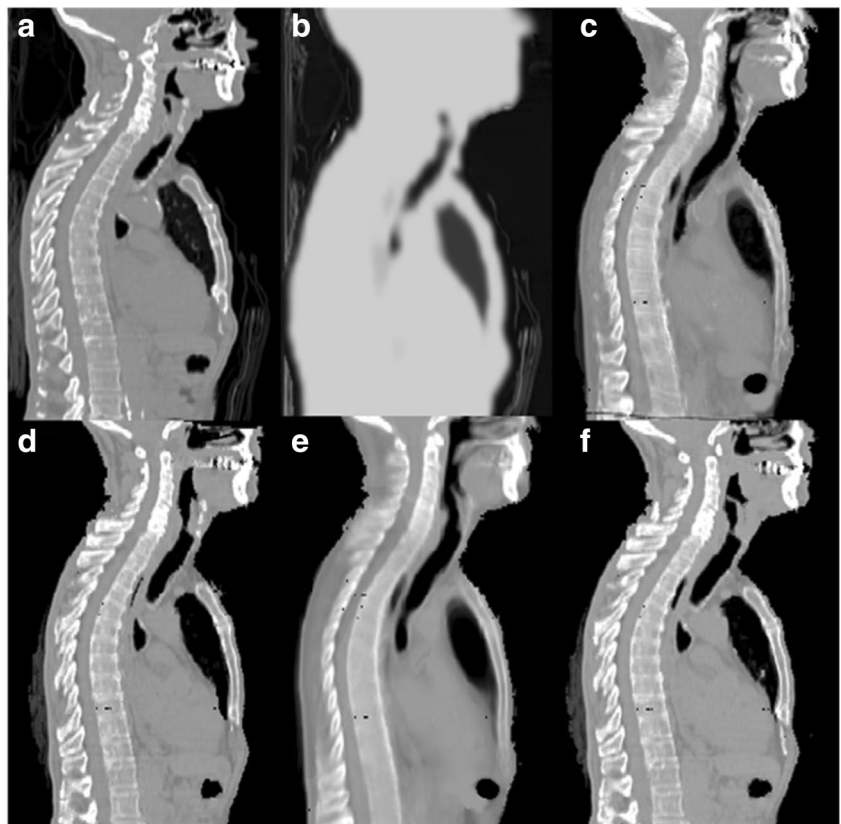


Table 1 Comparison of extracted bone accuracy validation measures (mean \pm SD) between the different pseudo-CT generation techniques, including Dice similarity (DSC), relative volume distance (RVD),Jaccard (JC), Sensitivity (S) and mean absolute surface distance (MASD). (*) indicates P-value > 0.05 according to the paired *t*-test

Methods	DSC	RVD (%)	JC	S	MASD (mm)
Average	0.60 \pm 0.02*	46.0 \pm 02.4*	0.43 \pm 0.02*	0.46 \pm 0.02*	10.7 \pm 03.9*
ORMA-average	0.55 \pm 0.03*	52.6 \pm 02.5*	0.38 \pm 0.02*	0.41 \pm 0.03*	11.3 \pm 03.6*
VWW	0.82 \pm 0.04	-09.0 \pm 04.1	0.75 \pm 0.04	0.77 \pm 0.04	02.0 \pm 01.1
ORMA-VWW	0.76 \pm 0.05	-16.8 \pm 05.4	0.66 \pm 0.05	0.69 \pm 0.06	03.9 \pm 01.8

registration plus VWW atlas fusion (PET_VWW), ORMA plus VWW atlas fusion (PET_ORMA-VWW), and the 3-class attenuation map (PET_MR3C). CT-based attenuation correction of PET data using CT (PET_ACCT) was considered as a reference for assessment of these techniques. Standardized uptake value (SUV) bias analysis was performed using volumes of interest (VOIs) defined on both normal uptake anatomical regions and malignant abnormalities split into soft-tissue and bone lesions. Soft-tissue lesions reside far from

bony structures whereas bone lesions are located in or very close to bones. An experienced nuclear medicine physician manually drew the VOIs on regions of normal physiologic uptake (lungs, liver, cerebellum, bone tissue (cervical vertebrae 6), aorta cross) and on malignant lesions located near and distant from bony structures. The differences between the various attenuation correction techniques were quantified in terms of changes in the SUV. The mean SUV measured in each VOI (PET_MRAC) was used to calculate the relative SUV bias (Eq. 7) and relative absolute SUV bias

Fig. 4 Representative slice of bone segmentation from MR images together with corresponding error distance map. **a** In-phase MR image, **(b)** corresponding CT image, **(c)** binary image of reference bone (extracted using a threshold of 180 HUs), **(d)** Average, **(e)** VWW, **(f)** ORMA-average, **(g)** ORMA-VWW

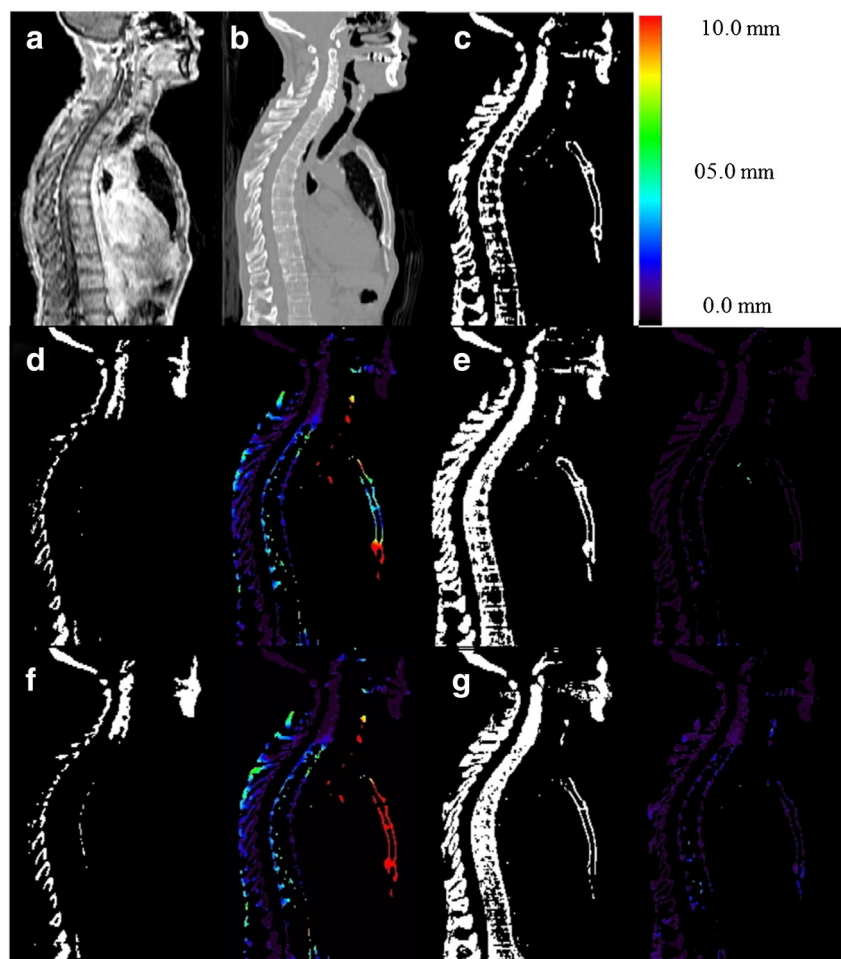


Table 2 Comparison of the accuracy of extracted air cavities in the head region between the different pseudo-CT generation techniques using different metrics, including Dice similarity (DSC), relative volume

Methods	DSC	RVD (%)	JC	S	MASD (mm)
Average	0.65±0.03	42.5±02.9*	0.47±0.03*	0.51±0.03*	1.2±01.6
ORMA-average	0.61±0.03	48.3±03.0*	0.42±0.03*	0.46±0.03*	1.4±01.8
VWW	0.83±0.04	08.2±03.8	0.77±0.04	0.78±0.05	00.5±00.8
ORMA-VWW	0.78±0.05	13.9±04.9	0.69±0.05	0.72±0.05	00.9±01.0

distance (RVD), Jaccard (JC), Sensitivity (S) and mean absolute surface distance (MASD). (*) indicates P-value > 0.05 according to paired *t*-test analysis

(Eq. 8) considering ACCT PET images (PET_ACCT) as reference:

Relative error (%)

$$= \frac{PET_MRAC(SUV) - PET_ACCT(SUV)}{PET_ACCT(SUV)} \times 100 (\%) \quad (7)$$

Relative absolute error (%)

$$= \frac{|PET_MRAC(SUV) - PET_ACCT(SUV)|}{PET_ACCT(SUV)} \times 100 (\%) \quad (8)$$

In addition to the calculated relative SUV errors, linear regression analysis results and joint histograms of MRI-derived attenuation maps versus reference CT images and PET/MRI-derived AC versus PET/CT were plotted for each technique (over all patients).

Results

The obtained two-dimensional projection of the coordinates is illustrated in Fig. 2. The origin of Fig. 2 indicates the location of the mean geometry, which is calculated by taking the arithmetic mean of 23 coordinates. The image residing at the closest location to the origin (atlas number 10) was chosen to be the best reference image.

Representative sagittal slices of the generated MRI-derived pseudo-CT images are shown in Fig. 3. These slices were chosen for visual assessment of bone extraction accuracy as

Table 3 Comparison of lung delineation accuracy between the different pseudo-CT generation techniques using standard validation measures (mean±SD): Dice similarity (DSC), relative volume distance

Methods	DSC	RVD (%)	JC	S	MASD (mm)
Average	0.87±0.05	07.1±02.9	0.78±0.03	0.81±0.02	9.7±06.6
ORMA-average	0.84±0.05	08.0±03.0	0.75±0.02	0.78±0.02	10.4±07.1
VWW	0.92±0.04	05.9±02.8	0.88±0.04	0.88±0.03	03.1±03.0
ORMA-VWW	0.90±0.04	06.6±02.9	0.85±0.04	0.85±0.03	03.9±03.4

well as the sharpness of the lungs and windpipe boundaries. Visual inspection revealed that the averaging atlas fusion method using either direct registration (Fig. 3c) or ORMA (Fig. 3e) tends to induce significant blurring and unsharpness compared to VWW (Fig. 3d and f, respectively). Table 1 summarizes bone extraction metrics between the different pseudo-CT generation methods. VWW atlas fusion approaches improve significantly all validation measures compared to averaging fusion (from 0.60 DSC to 0.82 DSC for direct registration). However, the accuracy is slightly compromised when employing ORMA (from 0.55 to 0.76 DSC). Figure 4 depicts representative binary masks of extracted bone when using the four pseudo-CT generation techniques together with their corresponding error distance map calculated through comparison with CT-derived bone (Fig. 4c). In addition, the evaluation of lung and air cavity segmentations revealed the same trend observed on bone extraction accuracy. The accuracy of air cavities delineation in the head region obtained from the different methods is slightly improved compared to bone results (Table 2). The VWW method resulted in air volume identification accuracy of 0.83 DSC while the ORMA approach resulted in 0.78 DSC. Table 3 compares the accuracy of lung volume delineation whereas Table 4 compares the mean attenuation coefficient of the lung expressed in Hounsfield units (HU) estimated by the different methods. The VWW approach not only enhances lung delineation accuracy and estimation of mean attenuation coefficients but also reduces the variability of the estimates. However, ORMA introduces moderate degradation of the results.

Table 5 (top) summarizes the relative errors between SUV_{mean} measured on PET images corrected for attenuation using four different atlas-based attenuation correction

(RVD), Jaccard (JC), Sensitivity (S) and mean absolute surface distance (MASD). There are no statistically significant differences between the results ($p < 0.05$) in all cases

Table 4 Comparison of lung attenuation in Hounsfield units (HUs) obtained from different methods

CT	MR3C	Average	ORMA-average	VWW	ORMA-VWW
-798 ± 54	-770 ± 00	-789 ± 70	-784 ± 79	-805 ± 57	-794 ± 62

methods together with the 3-class and CT-based attenuation-corrected PET images. The measured SUVs in bones (cervical 6) exhibit significant improvement from -29.3 ± 9.4 (PET_MR3C) to 3.4 ± 4.5 (PET_VWW) while a modest SUV recovery improvement is observed by exploiting direct atlas registration instead of the ORMA approach in almost all regions. Similarly, the relative absolute errors shown in Table 5 (bottom) show only slight degradation when applying the ORMA approach, even for bony lesions. The VWW-ORMA method resulted in an absolute error of 4.4 ± 4.3 compared to 4.0 ± 4.2 obtained using the VWW technique.

Figure 5 depicts the joint histogram graphs obtained by plotting the correlation between different MRI-derived attenuation maps and the reference CT image. The VWW scheme yielded the best regression correlation ($y = 1.02x + 0.2$ and $R^2 = 0.99$) while the 3-class attenuation map deviated substantially from the identity line ($y = 0.6x + 0.1$ and $R^2 = 0.72$). Applying the ORMA approach to the pseudo-CT generation process slightly degraded the correlation compared to the direct atlas registration framework. The same trend is seen in Fig. 6 where the joint histograms are plotted for PET tracer uptake values. PET images corrected for attenuation using the 3-class attenuation map underestimates tracer uptake while atlas-based techniques improved significantly quantitative

accuracy. Applying the ORMA approach as an alternative to direct atlas registration engendered a trivial deviation from tracer uptake values measured on PET/CT images. Figure 7 shows the error maps (relative bias) between reference CT images and five different MRI-derived attenuation maps for one representative clinical study. The estimated activity bias maps between PET/CT and PET images corrected for attenuation using five different attenuation maps of the same patient are illustrated in Fig. 8.

Discussion

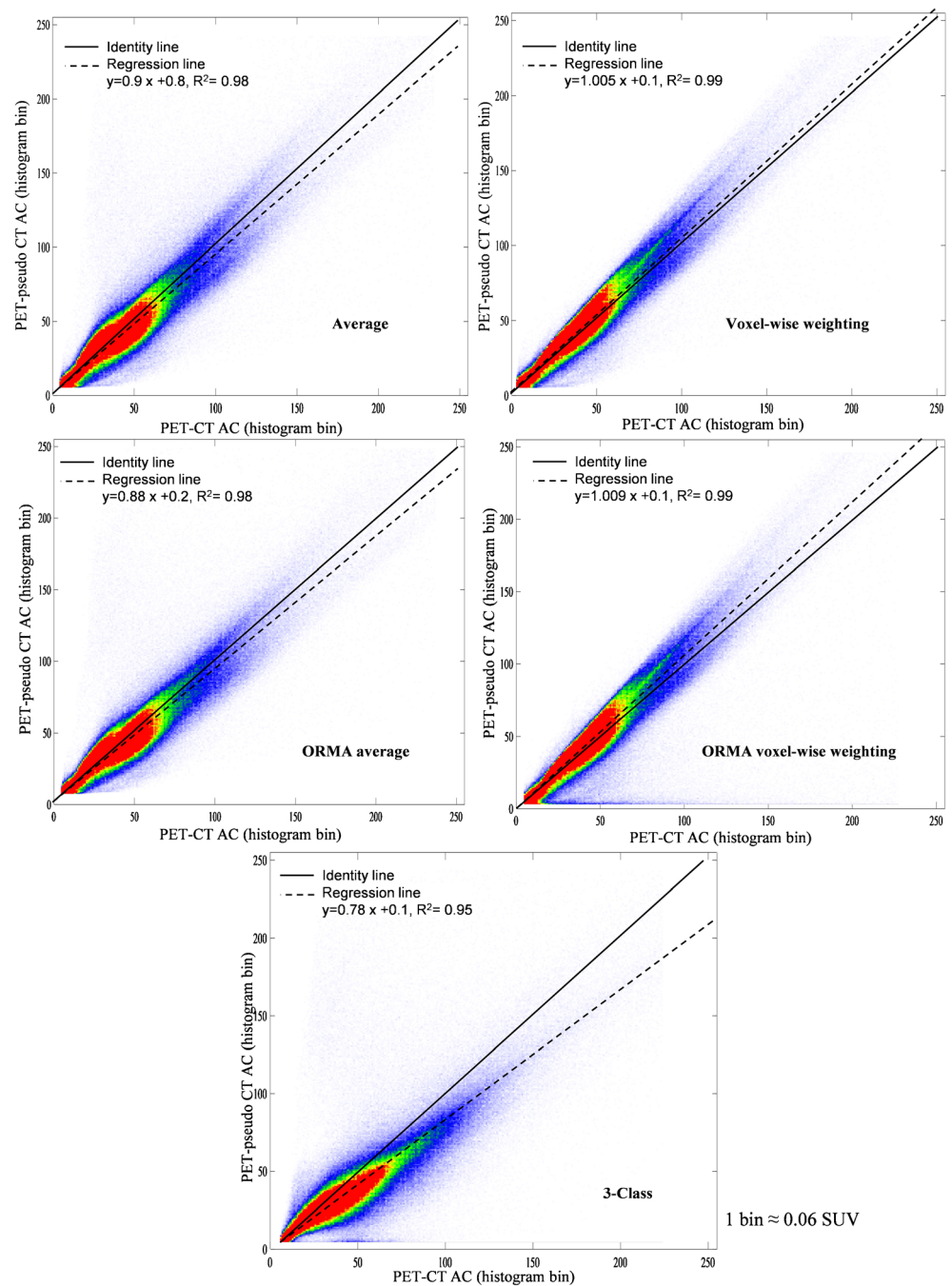
Employing the VWW scheme, whether applying the ORMA technique or not, had a remarkable impact on the quality of resulting pseudo-CT images in terms of extracted bone accuracy considering the validation measures summarized in Table 1. The inspection of Fig. 3 shows the superior quality of the VWW approach where the lung boundaries are remarkably sharper compared to simple averaging, which suffers from considerable diffusion of nearby soft-tissue. This would result in overestimation of tracer uptake in lung regions particularly near the boundaries. The resolved bony structures also exhibit major improvement in terms of anatomical details

Table 5 Relative errors (mean ± SD) (top) and relative absolute errors (mean ± SD) (bottom) between SUV_{mean} estimated using PET images corrected for attenuation using different MR-guided attenuation

Relative error	PET_Ave	PET_VWW	PET_ORMA-Ave	PET_ORMA-VWW	PET_MR3C
Cerebellum	-06.4 ± 6.8	03.3 ± 5.8	-05.9 ± 7.9	03.5 ± 6.1	-13.4 ± 6.0*
Lung	07.7 ± 10.4	-03.6 ± 8.7	10.8 ± 12.2	03.2 ± 9.8	18.6 ± 13.5*
Aorta cross	-05.1 ± 5.4	04.1 ± 4.5	-06.9 ± 6.1	04.3 ± 5.2	-16.6 ± 8.2*
Liver	-03.1 ± 4.8	03.9 ± 3.7	-04.6 ± 5.8	04.2 ± 4.4	-10.2 ± 6.7
Bone (cervical 6)	-09.4 ± 6.7	03.4 ± 4.5	-10.3 ± 7.1*	-04.9 ± 5.9	-29.3 ± 9.4*
Lesions (near bony structures)	-05.8 ± 6.1	01.4 ± 5.4	-05.7 ± 6.7	01.9 ± 5.9	-07.9 ± 7.2
Lesions (soft-tissue)	-02.7 ± 6.2	01.4 ± 5.2	-02.7 ± 6.5	-01.6 ± 5.8	-03.5 ± 8.2
Relative absolute error					
Cerebellum	9.3 ± 5.8	05.9 ± 4.6	09.5 ± 6.0	06.1 ± 5.2	15.6 ± 5.1
Lung	11.8 ± 9.1	06.4 ± 5.5	14.6 ± 10.0	06.7 ± 6.1	22.7 ± 12.2*
Aorta cross	07.9 ± 4.6	06.2 ± 3.6	08.8 ± 5.2	06.8 ± 4.3	20.0 ± 7.3
Liver	07.2 ± 3.9	05.9 ± 2.8	08.6 ± 4.5	06.7 ± 3.5	16.2 ± 5.8
Bone (cervical 6)	11.5 ± 5.7	06.3 ± 3.3	13.2 ± 6.2	07.9 ± 4.8	34.6 ± 8.4*
Lesions (near bony structures)	09.4 ± 5.3	04.0 ± 4.2	10.0 ± 5.9	04.4 ± 4.3	15.5 ± 6.7
Lesions (soft-tissue)	04.9 ± 4.3	03.7 ± 4.1	05.1 ± 4.8	04.2 ± 4.5	10.1 ± 7.8

correction approaches compared to CT-based attenuation correction serving as reference. (*) indicates P-value > 0.05 according to the paired t-test

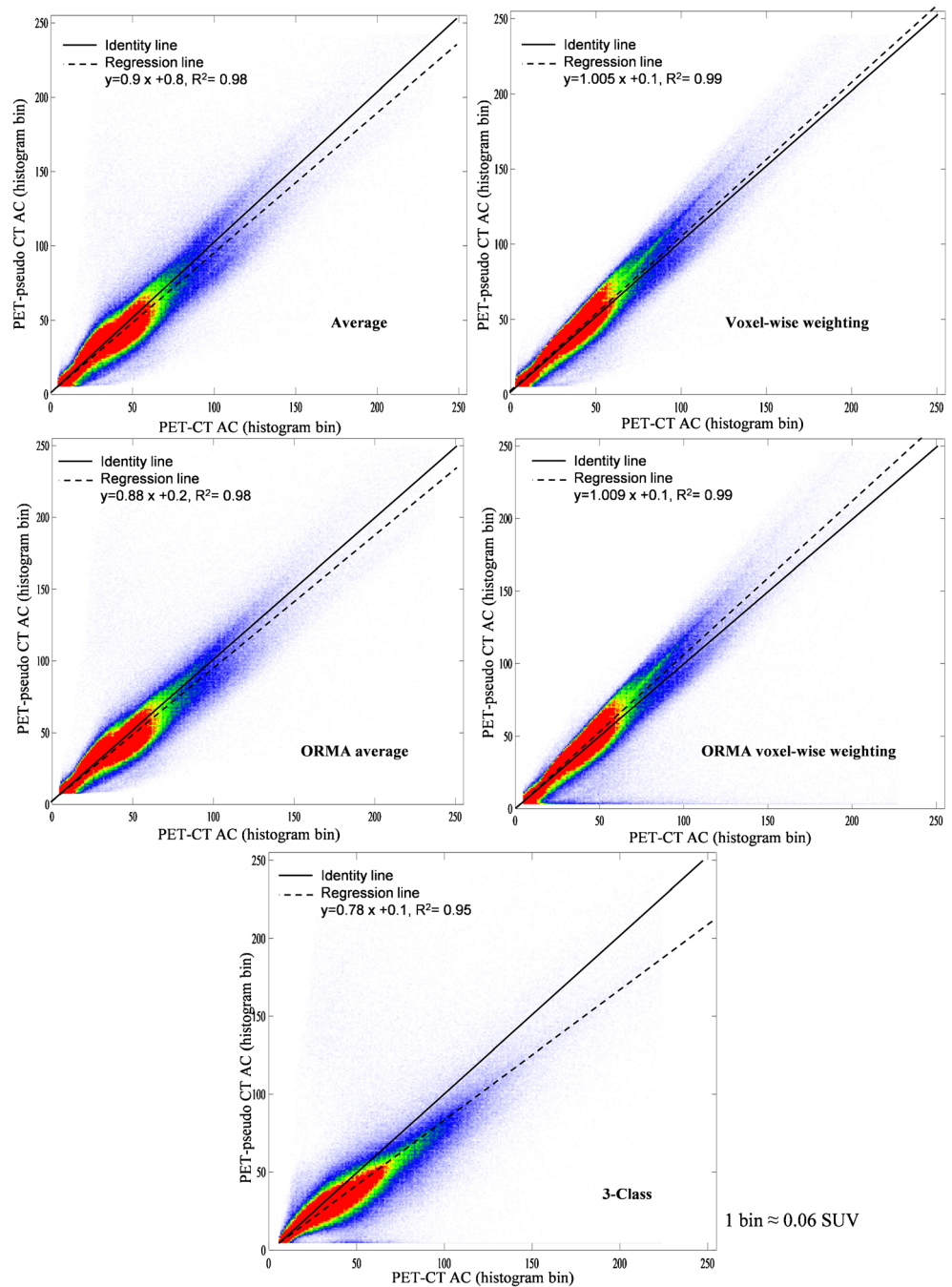
Fig. 5 Joint histograms correlating Average, VWW, ORMA-average, and ORMA-VWW pseudo-CTs with reference CT values. Each histogram bin corresponds almost to 16 HU



and boundary sharpness as reflected by the improvement of the Dice similarity measure from 0.60 ± 0.02 to 0.82 ± 0.04 and from 0.55 ± 0.03 to 0.76 ± 0.05 using direct registration and ORMA approaches, respectively. A plausible explanation for this improvement is that the local registration misalignment and anatomical variability are effectively handled by similarity weights and decent locally matched atlases contribute more to the resulting attenuation map. The same trend was observed in air cavities and lung delineation when applying

the VWW and ORMA schemes. However, predominant rigid motion in the head region caused slight improvement in air cavities delineation (0.83 ± 0.04 DSC) compared to bone (0.82 ± 0.04 DSC). Moreover, the enhanced accuracy in the lung delineation (0.92 ± 0.04 DSC) can partially be justified by the relatively large volume of the lung, which tends to reduce the impact of alignment errors. Similar improvement using local similarity weights were reported in atlas-based segmentation methods [31, 42] as well as

Fig. 6 Joint histograms correlating tracer uptake values from PET images corrected for attenuation using Average, VWW, ORMA-average, and ORMA-VWW pseudo-CT attenuation maps with CT-based PET attenuation-corrected images. Each histogram bin corresponds almost to 0.06 SUV

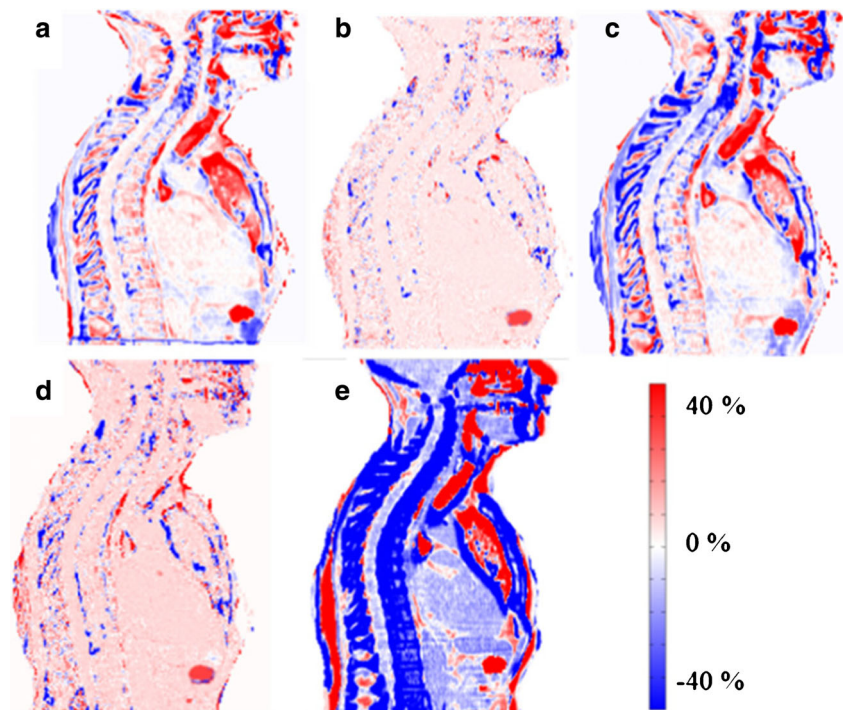


pseudo-CT generation in the head region [24, 43]. The regression analysis performed on the joint histogram of CT and pseudo-CT images revealed excellent correlation when using the VWW approach while the pseudo-CT obtained from arithmetic averaging led to significant deviation of the fitted regression line from the identity line. Since the 3-class attenuation map does not contain bone and the soft-tissue and lung classes are assigned uniform attenuation coefficients, the joint histogram shows two concentrated regions corresponding to lung and soft-

tissue predefined attenuation coefficients. These regions induce a large deviation from the reference line (Fig. 5).

The ORMA approach slightly degrades the quality of resulting pseudo-CT images when using either arithmetic averaging or VWW atlas fusion. The Dice validation measure reflecting bone extraction accuracy is reduced from 0.60 ± 0.02 to 0.55 ± 0.03 and from 0.82 ± 0.04 to 0.76 ± 0.05 , respectively. Yet, ORMA-VWW considerably outperforms arithmetic average of direct registration. It is worth noticing that computing and applying local weights adds negligible computational burden to

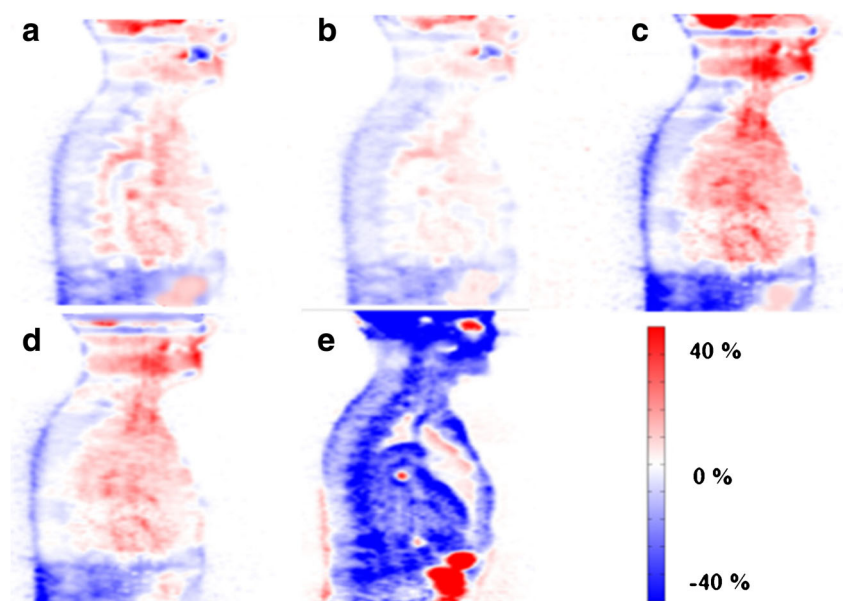
Fig. 7 Error maps (relative bias) between reference CT image and (a) Average, (b) VWW, (c) ORMA-average, (d) ORMA-VWW, and (e) MR-derived 3-class attenuation maps



the procedure, particularly when MSD is used as an image similarity measure that is considerably faster than other criteria, such as NMI and LNNC [49]. The bulk of computation time in multi-atlas-based segmentation or attenuation map generation methods is taken by the task of atlas-to-target registration consisting of N online image registrations. Depending on the registration algorithm, computer power, image size, and resolution, each non-rigid atlas registration may take about 10 min to 2 h (~1 h in this work). Furthermore, if unweighted averaging is the method of choice, increasing the number of atlas images beyond a certain

limit leads to an over-smoothed outcome since there is no currently implemented mechanism to discard poorly matched or anatomically different atlases. On the other hand, the use of too few atlas images suffers from statistical uncertainty [31, 42, 47]. In contrast, when employing the VWW framework, increasing the number of atlas images tends to improve the outcome since it increases the probability of finding appropriate local matches at the cost of increased computational time. The ORMA-VWW approach combines the advantage of selecting locally matched atlases with short computation time. The time needed for

Fig. 8 SUV error maps (relative bias) between PET_CTAC and (a) PET_Ave, (b) PET_VWW, (c) PET_ORMA-Ave, (d) PET_ORMA-VWW, and (e) PET_MR3C



performing ORMA is almost independent of the number of atlas images where only one online registration is carried out. This characteristic of ORMA makes it a promising option for potential combination with VWW atlas fusion. Although a slight degradation of quality is observed when using ORMA compared to direct registration, owing to imperfect serial image registration, the quality of the produced pseudo-CT images according to the joint histogram analysis and quantitative analysis of PET images is satisfactory for the purpose of PET attenuation correction.

In an attempt to reduce the computation time or number of required image registrations in atlas-based attenuation correction, Marshal et al. [29] proposed to select only the most similar atlas image based on meta-data, such as gender, weight, sex, and body mass index together with some image-derived features, such as fat to lean tissue ratio, body volume, lung volume, ...etc. The proposed method benefits from requiring only one image registration; however, the major drawback is its inability to take advantage of multi-atlas consensus to diminish the unsystematic bias imposed by each individual atlas image and inherent anatomical variability among subjects [42, 50].

The quantitative evaluation of SUV bias demonstrated a similar trend to that of attenuation maps. However, PET images show less sensitivity to errors in attenuation maps owing to lower spatial resolution and higher level of noise. The use of VWW attenuation maps did not lead to significant reduction of SUV bias in regions of interest (ROIs) defined on soft-tissue owing to the superiority of VWW over the averaging technique in terms of delineation of organ boundaries while the central parts of organs, where the ROIs were drawn, have almost similar attenuation coefficients. The same effect can also be observed for soft-tissue lesions located far away from bony structures. In this respect, the joint histogram plot and regression analysis are thought to be more descriptive since they offer a proper performance assessment of each technique. The MR3C technique resulted in significant SUV positive bias in the lung region (18.6 ± 13.5 % relative error and 22.7 ± 12.2 % absolute error) while the other approaches achieved relatively lower bias. The mean attenuation value of the lung determined by different methods (Table 4) explains the observed biases in the lung region. The MR3C method overestimated the average lung attenuation (-770 HU) while VWW schemes, with or without ORMA, produced values (-794 and -805 HU, respectively) close to those of reference CT (-798 HU).

According to Table 5 (top), PET-VWW achieved the best performance in terms of both mean bias and variability. The ORMA method slightly increases the mean bias and its variability. However, even when applying the ORMA method to VWW, the variability tends to be significantly lower than MR-3C, except in the cerebellum. The same trend is observed for PET-Ave and PET-ORMA-Ave where the mean and SD of the bias increases when applying the ORMA method. However, the SD of PET-ORMA-Ave is, in most of the regions (except the cerebellum), lower than PET-MR3C. Although, ORMA introduces a

trade-off between computation time and the achieved accuracy of the generated attenuation maps, the overall performance is improved compared to the 3-class attenuation map even when using the ORMA-Ave method. The VWW scheme resulted in relative absolute errors of less than 10 % in all regions even when utilizing the accelerated ORMA approach.

The quantitative analysis of PET images did not reveal a significant difference between VWW and ORMA-VWW pseudo-CT attenuation maps whereas the computation time for generation of ORMA-VWW pseudo-CT is almost $1/N$ th (N is the number of used atlas images) that of direct registration VWW method. The attractive feature of the ORMA approach is that by increasing the number of atlas images, the computation time does not change significantly. The technique is time efficient and promising for use in clinical routine compared to that of the direct registration approach.

Conclusion

In this work, we proposed an atlas-based pseudo-CT generation technique for whole-body imaging requiring only one online registration, regardless of number of atlas images, integrated within a voxel-wise atlas fusion framework. The proposed method generates acceptable PET attenuation maps with a Dice similarity of 0.76 ± 0.05 for extracted bone compared to 0.82 ± 0.04 achieved by the conventional atlas-based method, which entails lengthy N (number of used atlas images) image registrations. The quantitative analysis revealed good correlation between PET images corrected for attenuation using the proposed pseudo-CT algorithm and the corresponding reference CT images. Despite the modest loss of accuracy, the required computation time is reduced by factor N , thus enabling the clinical implementation of the technique.

Acknowledgments This work was supported by the Swiss National Science Foundation under grant SNFN 31003A-149957.

Compliance with ethical standards

Conflict of interest The authors declare that they have no conflicts of interest.

Disclosure of potential conflicts of interest None of the authors have affiliations that present financial or non-financial competing interests for this work.

Research involving human participants All procedures performed in studies involving human participants were in accordance with the ethical standards of the institutional and/or national research committee and with the 1964 Helsinki declaration and its later amendments or comparable ethical standards.

Informed consent Informed consent was obtained from all individual participants included in the study.

Appendix The geometric distances obtained from pair-wise registrations are used to form an $N \times N$ distance matrix (D) (whose elements d_{ij} stand for geometric distances between objects i and j) to be processed by multidimensional scaling (MDS). The purpose of the MDS technique is to provide relative spatial locations from a set of pair-wise distances [41]. Since the distance used in MDS does not necessarily need to be metric or based on a system of standard measurements (any set of arbitrary values can be used), the geometric distances calculated from pair-wise registration are valid for use by the MDS procedure. MDS produces a number of coordinates in a user-defined dimension based on the Eigen structure of the distance matrix. Here, we transformed the distance matrix into two most meaningful coordinates computed by MDS where the closest subject to the origin represents the reference image, which is the closest to the mean geometry of the population of subjects using the following procedure:

1. The matrix B is computed considering $B = -\frac{1}{2}JD^2J$ using the matrix $= I - N^{-1}11'$, where N is the number of subjects, I is the identity matrix and $11'$ denotes a square matrix of ones.
2. The two largest Eigenvalues λ_1 and λ_2 of B and the corresponding two Eigenvectors are extracted,
3. A 2-dimensional spatial configuration of the N subjects is derived from the coordinate matrix $X = E_2 C_2^{1/2}$, where E_2 is the matrix of 2 Eigenvectors and C_2 is the diagonal matrix of 2 Eigenvalues of B , respectively.
4. The subject residing at the minimum distance to the origin in the new coordinate space is defined as the reference image (Fig. 2).

References

1. Judenhofer MS, Wehrl HF, Newport DF, Catana C, Siegel SB, Becker M, et al. Simultaneous PET-MRI: a new approach for functional and morphological imaging. *Nat Med*. 2008;14:459–65.
2. Zaidi H, Del Guerra A. An outlook on future design of hybrid PET/MRI systems. *Med Phys*. 2011;38:5667–89.
3. Wiesmuller M, Quick HH, Navalpakkam B, Lell MM, Uder M, Ritt P, et al. Comparison of lesion detection and quantitation of tracer uptake between PET from a simultaneously acquiring whole-body PET/MR hybrid scanner and PET from PET/CT. *Eur J Nucl Med Mol Imaging*. 2013;40:12–21.
4. Becker M, Zaidi H. Imaging in head and neck squamous cell carcinoma: the potential role of PET/MRI. *Br J Radiol*. 2014;87:20130677.
5. Spick C, Herrmann K, Czernin J. 18F-FDG PET/CT and PET/MRI perform equally well in cancer patients: evidence from studies in more than 2300 patients. *J Nucl Med*. 2016;57:420–30.
6. Bezrukov I, Mantlik F, Schmidt H, Scholkopf B, Pichler BJ. MR-based PET attenuation correction for PET/MR imaging. *Semin Nucl Med*. 2013;43:45–59.
7. Mehranian A, Arabi H, Zaidi H. Vision 20/20: magnetic resonance imaging-guided attenuation correction in PET/MRI: challenges, solutions, and opportunities. *Med Phys*. 2016;43:1130–55.
8. Zaidi H, Montandon M-L, Slosman DO. Magnetic resonance imaging-guided attenuation and scatter corrections in three-dimensional brain positron emission tomography. *Med Phys*. 2003;30:937–48.
9. Martinez-Moller A, Souvatzoglou M, Delso G, Bundschuh RA, Chefid'hotel C, Ziegler SI, et al. Tissue classification as a potential approach for attenuation correction in whole-body PET/MRI: evaluation with PET/CT data. *J Nucl Med*. 2009;50:520–6.
10. Schulz V, Torres-Espallardo I, Renisch S, Hu Z, Ojha N, Bömert P, et al. Automatic, three-segment, MR-based attenuation correction for whole-body PET/MR data. *Eur J Nucl Med Mol Imaging*. 2011;38:138–52.
11. Montandon M-L, Zaidi H. Atlas-guided non-uniform attenuation correction in cerebral 3D PET imaging. *Neuroimage*. 2005;25:278–86.
12. Hofmann M, Bezrukov I, Mantlik F, Aschoff P, Steinke F, Beyer T, et al. MRI-based attenuation correction for whole-body PET/MRI: quantitative evaluation of segmentation- and Atlas-based methods. *J Nucl Med*. 2011;52:1392–9.
13. Arabi H, Zaidi H. Magnetic resonance imaging-guided attenuation correction in whole-body PET/MRI using a sorted atlas approach. *Med Image Anal*. 2016;31:1–15.
14. Keereman V, Fierens Y, Broux T, De Deene Y, Lonneux M, Vandenberghe S. MRI-based attenuation correction for PET/MRI using ultrashort echo time sequences. *J Nucl Med*. 2010;51:812–8.
15. Berker Y, Franke J, Salomon A, Palmowski M, Donker HC, Temur Y, et al. MRI-based attenuation correction for hybrid PET/MRI systems: a 4-class tissue segmentation technique using a combined Ultrashort-Echo-Time/Dixon MRI sequence. *J Nucl Med*. 2012;53:796–804.
16. Delso G, Wiesinger F, Sacolick L, Kaushik S, Shanbhag D, Hullner M, et al. Clinical evaluation of zero echo time MRI for the segmentation of the skull. *J Nucl Med*. 2015;56:417–22.
17. Rezaei A, Defrise M, Bal G, Michel C, Conti M, Watson C, et al. Simultaneous reconstruction of activity and attenuation in time-of-flight PET. *IEEE Trans Med Imag*. 2012;31:2224–33.
18. Mehranian A, Zaidi H. Joint estimation of activity and attenuation in whole-body TOF PET/MRI using constrained Gaussian mixture models. *IEEE Trans Med Imaging*. 2015;34:1808–21.
19. Izquierdo-Garcia D, Hansen AE, Forster S, Benoit D, Schachoff S, Furst S, et al. An SPM8-based approach for attenuation correction combining segmentation and nonrigid template formation: application to simultaneous PET/MR brain imaging. *J Nucl Med*. 2014;55:1825–30.
20. Schreiber E, Nye JA, Schuster DM, Martin DR, Votaw J, Fox T. MR-based attenuation correction for hybrid PET-MR brain imaging systems using deformable image registration. *Med Phys*. 2010;37:2101–9.
21. Fei B, Yang X, Nye JA, Aarsvold JN, Raghunath N, Cervo M, et al. MRPET quantification tools: registration, segmentation, classification, and MR-based attenuation correction. *Med Phys*. 2012;39:6443–54.
22. Hofmann M, Steinke F, Scheel V, Charpiat G, Farquhar J, Aschoff P, et al. MRI-based attenuation correction for PET/MRI: a novel approach combining pattern recognition and Atlas registration. *J Nucl Med*. 2008;49:1875–83.
23. Malone IB, Ansorge RE, Williams GB, Nestor PJ, Carpenter TA, Fryer TD. Attenuation correction methods suitable for brain imaging with a PET/MRI scanner: a comparison of tissue atlas and template attenuation map approaches. *J Nucl Med*. 2011;52:1142–9.
24. Burgos N, Cardoso M, Thielemans K, Modat M, Schott J, Duncan J, et al. Attenuation correction synthesis for hybrid PET-MR scanners: application to brain studies. *IEEE Trans Med Imaging*. 2014;33:2332–41.
25. Sjölund J, Forsberg D, Andersson M, Knutsson H. Generating patient specific pseudo-CT of the head from MR using atlas-based regression. *Phys Med Biol*. 2015;60:825–39.

26. Mehranian A, Arabi H, Zaidi H. Quantitative analysis of MRI-guided attenuation correction techniques in time-of-flight brain PET/MRI. *Neuroimage*. 2016;130:123–33.
27. Bezrukov I, Schmidt H, Mantlik F, Schwenzer N, Brendle C, Scholkopf B, et al. MR-based attenuation correction methods for improved PET quantification in lesions within bone and susceptibility artifact regions. *J Nucl Med*. 2013;54:1768–74.
28. Hermosillo G, Raykar V, Zhou X. Learning to locate cortical bone in MRI. In: Wang F, Shen D, Yan P, Suzuki K, editors. *Machine learning in medical imaging*. Berlin: Springer; 2012. p. 168–75.
29. Marshall HR, Patrick J, Laidley D, Prato FS, Butler J, Theberge J, et al. Description and assessment of a registration-based approach to include bones for attenuation correction of whole-body PET/MRI. *Med Phys*. 2013;40:082509
30. Uh J, Merchant TE, Li Y, Li X, Hua C. MRI-based treatment planning with pseudo CT generated through atlas registration. *Med Phys*. 2014;41:051711–8.
31. Arabi H, Zaidi H. Comparison of atlas-based bone segmentation methods in whole-body PET/MRI. *IEEE Nuclear Science Symposium and Medical Imaging Conference (NSS/MIC)*. Seattle, WA, USA; 2014.
32. Zaidi H, Ojha N, Morich M, Griesmer J, Hu Z, Maniowski P, et al. Design and performance evaluation of a whole-body Ingenuity TF PET-MRI system. *Phys Med Biol*. 2011;56:3091–106.
33. Klein S, Staring M, Murphy K, Viergever MA, Pluim JPW. elastix: a toolbox for intensity-based medical image registration. *IEEE Trans Med Imaging*. 2010;29:196–205.
34. Arabi H, Rager O, Alem A, Varoquaux A, Becker M, Zaidi H. Clinical assessment of MR-guided 3-class and 4-class attenuation correction in PET/MR. *Mol Imaging Biol*. 2015;17:264–76.
35. Perona P, Malik J. Scale-space and edge detection using anisotropic diffusion. *IEEE Trans Pattern Analy Machine Intell*. 1990;12:629–39.
36. Tustison NJ, Avants BB, Cook PA, Zheng Y, Egan A, Yushkevich PA, et al. N4ITK: improved N3 bias correction. *IEEE Trans Med Imaging*. 2010;29:1310–20.
37. McAuliffe MJ, Lalonde FM, McGarry D, Gandler W, Csaky K, Trus BL. *Medical Image Processing, analysis and visualization in clinical research*. Proceedings 14th IEEE Symposium on Computer-Based Medical Systems, CBMS. 2001. pp. 381–6.
38. Mattes D, Haynor DR, Vesselle H, Lewellen TK, Eubank W. PET-CT image registration in the chest using free-form deformations. *IEEE Trans Med Imaging*. 2003;22:120–8.
39. Park H, Bland PH, Hero 3rd AO, Meyer CR. Least biased target selection in probabilistic atlas construction. *Med Image Comput Comput Assist Interv*. 2005;8:419–26.
40. Bookstein FL. Principal warps: thin-plate splines and the decomposition of deformations. *IEEE Trans Pattern Analy Machine Intell*. 1989;11:567–85.
41. Young FW, Hamer RM. *Multidimensional scaling: history, theory, and applications*. New York: Taylor & Francis; 1987.
42. Artaechevarria X, Munoz-Barrutia A, Ortiz-de-Solorzano C. Combination strategies in multi-atlas image segmentation: application to brain MR data. *IEEE Trans Med Imaging*. 2009;28:1266–77.
43. Burgos N, Cardoso MJ, Modat M, Pedemonte S, Dickson J, Barnes A, et al. Attenuation correction synthesis for hybrid PET-MR scanners. *Med Image Comput Comput Assist Interv*. 2013;16:147–54.
44. Yushkevich PA, Wang H, Pluta J, Das SR, Craige C, Avants BB, et al. Nearly automatic segmentation of hippocampal subfields in in vivo focal T2-weighted MRI. *Neuroimage*. 2010;53:1208–24.
45. Dice LR. Measures of the amount of ecologic association between species. *Ecology*. 1945;26:297–302.
46. Xia Y, Fripp J, Chandra SS, Schwarz R, Engstrom C, Crozier S. Automated bone segmentation from large field of view 3D MR images of the hip joint. *Phys Med Biol*. 2013;58:7375–90.
47. Heckemann RA, Hajnal JV, Aljabar P, Rueckert D, Hammers A. Automatic anatomical brain MRI segmentation combining label propagation and decision fusion. *Neuroimage*. 2006;33:115–26.
48. Yushkevich PA, Piven J, Hazlett HC, Smith RG, Ho S, Gee JC, et al. User-guided 3D active contour segmentation of anatomical structures: significantly improved efficiency and reliability. *Neuroimage*. 2006;31:1116–28.
49. Lötjönen JMP, Wolz R, Koikkalainen JR, Thurfjell L, Waldemar G, Soininen H, et al. Fast and robust multi-atlas segmentation of brain magnetic resonance images. *Neuroimage*. 2010;49:2352–65.
50. Rohlfing T, Brandt R, Menzel R, Maurer Jr CR. Evaluation of atlas selection strategies for atlas-based image segmentation with application to confocal microscopy images of bee brains. *Neuroimage*. 2004;21:1428–42.